P and S wave velocities of consolidated sediments from a seafloor seismic survey in the North Celtic Sea Basin, offshore Ireland

Donna J. Shillington[1], Timothy A. Minshull[1], Christine Peirce[2], John M. O'Sullivan[3]

[1]National Oceanography Centre, Southampton, University of Southampton, European Way, Southampton SO14 3ZH, UK

[2]Department of Earth Sciences, Durham University, Durham, DH1 3LE, UK

[3]Providence Resources Plc, Airfield House, Airfield Park, Donnybrook, Dublin 4, Ireland

Keywords: multicomponent sensors, ocean bottom seismographs, V_P/V_S ratio, velocity modeling

Abstract

A geophysical survey was conducted over a hydrocarbon prospect in the North Celtic Sea Basin using a small array of ocean-bottom seismographs (OBSs). The purpose of this study was to determine the ratio of (P) compressional- to (S) shear-wave velocity of consolidated sedimentary rocks in order to constrain possible subsurface variations in pore-fluid content. The ratio of V_P and V_S is known to be particularly sensitive to lithology, porosity and pore-fluid content, making it a useful parameter for evaluating hydrocarbon prospects. OBSs offer a relatively cheap and time-effective means of acquiring multi-component data compared with ocean-bottom cables, but they have not often been used by the hydrocarbon industry to characterize physical properties in the shallow subsurface. In this contribution, we demonstrate the ability of an OBS survey comprising three pairs of two OBSs spaced at 1.6 km to recover lateral variations in the V_P/V_S ratio. A key requirement of this type of study is that S-waves will be generated by mode conversions in the subsurface, since they cannot be generated in nor travel through fluids. In this survey, the contrast in physical properties of the hard seabed of the North Celtic Sea Basin provided a means of generating converted S-waves. Two-dimensional ray-tracing and forward modeling was used to create both V_P and V_S models along a profile crossing the Blackrock prospect in the North Celtic Sea Basin. These models comprise four layers and extend to a maximum depth of 1.1 km. The observed northward decrease in the V_P/V_S ratio at depths of 500-1000 m below the seafloor in the study area is interpreted to represent lateral variation in the amount of gas present in the pore space of Upper Cretaceous chalks and shales overlying the prospective reservoir.

Introduction

Geoscientists in academia and industry have increasingly recognized the value of shear (S)-waves in placing constraints on subsurface variations in lithology, porosity and pore-fluid content. The interpretation of these characteristics from compressional (P)-wave velocities in the absence of other data is ambiguous. However, because P- and S-wave velocities (V_P and V_S, respectively) are controlled by different elastic properties of a given rock, the inclusion of S-waves in data analysis and modeling can significantly reduce the ambiguity associated with interpreting seismic data. For example, the shear modulus of a fluid is close to zero, so that V_S is not as sensitive to variations in pore fluid content as V_P (Gregory, 1976). Consequently, the ratio of V_P to V_S (V_P/V_S) is a useful means of jointly interpreting these two types of seismic information to assess not only subsurface lithological properties, but also the nature of the porosity and its contents. For example, a typical V_P/ V_S ratio for sandstone is ~1.6-1.75 and for limestone is ~1.85-1.95 (Pickett, 1963), while for shales V_P/V_S is usually >2.0 (Tatham, 1985). The presence of hydrocarbons, particularly gas, in the pore space instead of water tends to cause a decrease of as much as 10-20 percent in V_P/ V_S (Gregory, 1976).

Although the analysis of S-wave data can significantly reduce the uncertainty in interpreting seismic data, such data are also more difficult to collect, particularly in marine settings. Towed seismic streamers can record converted waves that contain information on S-wave velocities, but these arrivals are usually very weak because two mode conversions are required (i.e., a P- to S-wave conversion of down-going seismic energy at the seabed and S- to P-wave conversion of returning seismic energy). As a result, it is necessary to deploy multi-component receivers on the seabed to record S-wave arrivals whose amplitudes are high enough such that these phases can be identified and analyzed. The energy industry typically acquires

multi-component data by installing ocean-bottom cables at significant cost, which require significant time to deploy and recover. Furthermore, even when S-wave data are collected, their analysis is often applied to specific objectives, such as imaging features below gas accumulations (Knapp *et al.*, 2002), rather than estimating variations in lithology and pore-fluid contents by creating and interpreting velocity models derived from multi-component data (Garotta *et al.*, 2002; Roy *et al.*, 2002).

An alternative approach to collecting S-wave data is via the use of ocean-bottom seismographs (OBSs) (Jin *et al.*, 2000; Mjelde *et al.*, 2003). These are individual stations (rather than a cable containing many stations) and can be deployed and recovered from a vessel without specialized equipment, in contrast to ocean-bottom cables, which are usually installed using divers or remotely operated vehicles (ROVs). Consequently, OBSs are much cheaper and quicker to utilize. Furthermore, OBSs have underpinned marine academic research into sedimentary and crustal structure for the past ~30 years, resulting in the development of a wide variety of software packages for analyzing the resulting data using either forward modeling or inversion (e.g., Zelt and Barton, 1998; Zelt and Smith, 1992). The hydrocarbon industry has also successfully used OBSs to image large-scale structures, such as variations in crustal thickness or to determine crustal type (Hughes *et al.*, 1998), or for sub-basalt imaging (Spitzer *et al.*, 2005). However, OBSs have not been applied as often by industry for smaller-scale studies of sedimentary lithology and pore-content estimation (Jin *et al.*, 2000).

In this paper, we present the results of 2D velocity analysis based on an array of six OBSs deployed in pairs (for redundancy of acquisition) spaced at 1.6 km intervals along a NNW-SSE line crossing the Blackrock prospect in the northern Celtic Sea. Blackrock is thought to be a possible fault-bound reservoir (Line 1, Fig. 1). This study was designed to test the ability of a

simple OBS array to characterize lateral variations in both V_P and V_S in a shallow reservoir setting and, in turn, assess the suitability of the approach in predicting fluid versus gas pore contents within potential reservoir structures interpreted in marine multichannel seismic reflection data. Another advantage of conducting this study at the Blackrock prospect is that some well data are available with which our results can be calibrated. Given that the lithology and porosity of stratigraphic units in this region are well known from nearby wells, the contributions of lithology, porosity and pore-fluid content to any observed lateral variations in the V_P/ V_S ratio at the Blackrock prospect can be assessed.

Regional geology and petroleum system

The Blackrock prospect is a dip and fault bounded structure located 80 km from the south coast of Ireland within the ENE-WSW oriented North Celtic Sea Basin (~100 m water depth). This is one of a series of basins around Ireland that opened in response to extension in the Early-Late Triassic, before the opening of the North Atlantic at this latitude (Shannon and Naylor, 1998). The orientation of these basins is significantly controlled by pre-existing structures from the Caledonian and Variscan orogenies (Rowell, 1995). This region later experienced uplift in the Paleocene/Eocene associated with the formation of the North Atlantic Volcanic Province and in the Oligo-Miocene as a result of the Alpine orogeny, resulting in the formation of inversion structures throughout the North Celtic Sea Basin (Murdoch *et al*., 1995). Many of the economically viable fields in the North Celtic Sea Basin have been discovered by drilling such inversion structures, including Kinsale Head, Ballycotton, SW Kinsale, and Seven Heads (Shannon and Naylor, 1998); the Blackrock prospect also falls into this category.

69 The stratigraphy in the basin is summarized briefly below and illustrated in Fig. 2a, and a
70 detailed description can be found in Shannon and Naylor (1998). The basement comprises
71 Devonian and Carboniferous strata deformed during the Variscan orogeny. This basement is
72 overlain by a Triassic and Jurassic succession that includes the primary source rocks of the North
73 Celtic Sea Basin; these units are not discussed further as they are not imaged by the present
74 study. The Wealden formation unconformably overlies the Late Jurassic section, and comprises
75 Early Cretaceous sandy non-marine and marine sediments. The Wealden is one of the reservoir
76 formations in this region as a whole, and in the vicinity of the Blackrock prospect in particular.
77 This unit is unconformably overlain by the Greensand Group (Albian), which contains another
78 reservoir rock in the North Celtic Sea Basin (e.g., 'A' Sand Formation at Kinsale and
79 Ballycotton) (Taber *et al.*, 1995). The 'A' Sand Formation is as thick as ~50 m near the Kinsale
80 discovery, but thins to ~10 m near the Blackrock prospect (Taber *et al.*, 1995). This unit is
81 conformably overlain by Albian and Cenomanian limestones and claystones, Upper Cretaceous
82 chalks and clays (which serve as a potential seal) and Cenozoic non-marine units including
83 sandstones and shales.
84 A relevant attribute of the geology of this region is the existence of a hard seabed, where
85 the shallowest sedimentary layers are associated with relatively high seismic velocities. The
86 abrupt contrast in physical properties at the seabed presents a likely means of generating P- to S-
87 wave mode conversions necessary to calculate V_S structure and the V_P/V_S ratio (Spudich and
88 Orcutt, 1980). This characteristic likely results from the removal of ~400-700 km of sediment in
89 this area during Cenozoic uplift events (Murdoch *et al.*, 1995), which would place older, more
90 indurated sedimentary rocks at the seafloor. Further modification of the seabed likely occurred
91 during the Last Glacial Maximum, which resulted in the deposition of the Irish Sea Till in the

92 Celtic Sea as far south as ~49º30'N (Ó Cofaigh and Evans, 2007). Site survey data from the area
93 of the Blackrock prospect indicate that Cretaceous chalks are overlain by up to ~10 m of coarse
94 material, which likely corresponds to the Irish Sea Till, and up to ~4 m of younger fine-grained
95 sand. Outcrops of chalk are observed at the seafloor to the south. Despite this recent deposition,
96 the seabed will still represent an abrupt change in properties in this dataset because the dominant
97 frequencies of our data are 15-25 Hz, which correspond to wavelengths of 60-200 m assuming
98 velocities between 1500-3000 m/s.
99 Several wells have already been drilled in the area of the Blackrock prospect. IRL48/30-
100 1 was drilled in 1973 to a total depth of ~2900 m (Figs. 1 and 2), and this well encountered oil in
101 the Upper and Middle Wealden sands and gas charged zones in the Lower Jurassic unit.
102 Providence Resources drilled a second well in the Blackrock area in 2004 (IRL49/26-1A, Fig. 1),
103 but no significant shows were observed in the target Wealden sands. Post-drilling analysis
104 suggested that a basin shoulder fault (Figs. 1 and 2b) might be controlling the hydrocarbon
105 system, such that drilling on the opposite (northern basinward) side of the fault might prove more
106 successful. The estimation of V_P/V_S from OBS data presented in this paper was designed to test
107 this hypothesis and assess likely reservoir and well viability by predicting pore fluid content
108 prior to any subsequent drilling.
109
110 **Acquisition and processing**
111 In November 2006, six OBSs were deployed along a NNW-SSE dip-oriented transect
112 across the Blackrock prospect in the Celtic Sea from the M/V *Sea Surveyor* (Fig. 1). The OBSs
113 were deployed in three pairs (to provide acquisition redundancy) with ~1.6 km separating each
114 pair. OBSs were supplied by the Ocean-Bottom Instrumentation Consortium (OBIC), a

115 partnership between Durham University, the University of Southampton, and Imperial College.
116 The sensors were a hydrophone and three orthogonal 4.5 Hz geophones in a gimbaled pressure
117 case, which is mounted directly at the base of the instrument frame Signals from these sensors
118 were logged at 250 Hz.

119 Following deployment, the M/V *Sea Surveyor* shot two lines, one NNW-SSE across all
120 of the OBSs (Line 1, Fig. 1), and a second orthogonal line that crossed Line 1 at OBS 3 (Line 2,
121 Fig. 1). Additionally, squares were shot around each pair of OBSs for the purpose of relocating
122 and orienting the horizontal sensor components (Fig. 1). The source consisted of six Bolt 1900ll
123 airguns, with four of the guns arranged in clustered pairs. The total array volume was 470 in^3.
124 The guns were towed at a nominal depth of 4 m. Source modeling prior to the survey indicated
125 that this airgun configuration would produce a source signature with significant energy at 10-180
126 Hz. Shots were fired on distance at a spacing of 12.5 m. Only ~24 hrs were required to shoot
127 the two cross lines and squares around each instrument, such that the OBSs were only deployed
128 for a maximum of ~30 hrs.

129 Multi-channel seismic (MCS) reflection data were also acquired contemporaneously
130 along Lines 1 and 2 with a 600 m, 48-channel Teledyne streamer towed at a depth of 5 m. The
131 MCS data sampling interval was 1 ms, and the record length was 4 s two-way traveltime
132 (TWTT). The streamer data were not directly incorporated in the present analysis, but we
133 compare the results of our modeling with features observed in initial migrations of these data,
134 which were provided by Gardline Geosurvey Ltd, in the Discussion.

135 Prior to OBS data interpretation and modeling, processing steps were undertaken to 1)
136 correct shot times, 2) determine correct instrument locations on the seabed, 3) orient the
137 horizontal sensor components relative to the shot lines, and 4) filter the data to improve signal-

to-noise characteristics for phase identification and traveltime picking. A critical piece of information for successful analysis of OBS data is a record of shot times accurate to the sampling interval (±4 ms in this case). We recorded times from two GPS clocks, shot triggers and shot instances on a data logger. These times were then used to organize the data recorded on each OBS, which were stored as a single continuous trace for each channel, into individual traces associated with each shot. Linear corrections are also applied for clock drift by comparing the internal clocks in the OBSs with the GPS clock; because the OBSs were only deployed for a very short period of time (~30 hrs), drift corrections were very small (1.5-4.5 ms).

The second step is to determine the locations and orientations of the OBS on the seafloor. Although the exact location at the sea surface where each instrument was deployed is known, the instrument can drift away from this location as it descends through the water column to the seafloor on deployment and ascends through the water column on recovery. Direct water wave arrival times from all shots are used to accurately determine the position of each OBS. Direct arrivals occur as first arrivals to offsets of ~150 m, but can be observed as secondary arrivals to larger source-receiver offsets.

As this study is concerned with S-wave arrivals, it is also important to determine the orientation of the orthogonal horizontal geophone components relative to the shot lines. This can be done by determining the azimuths at which polarity changes in the direct water wave arrivals on the horizontal geophone components occur using the shots from squares shot around each pair of instruments (Fig. 1). Once the orientations are known, the horizontal components can be transformed into radial and transverse components. For isotropic or weakly anisotropic media, the radial component will contain much more energy than the transverse component, thus facilitating the identification of S-wave arrivals.

Finally, the data were filtered in order to enhance both P- and S-wave reflections and refractions for phase identification. This was accomplished by applying a minimum-phase Butterworth band-pass filter with corner frequencies of 1, 2, 40, 50 Hz. We also applied a minimum-phase spiking deconvolution to whiten the frequency spectra. Fig. 3 shows an example of data from OBS 4 whose location is shown in Fig. 1.

Phase interpretation and modeling

Both P-wave and S-wave arrivals were observed on all of the OBSs deployed for this study (e.g., Fig. 3). Refractions are divided into phases based on differences in their apparent velocities and the presence of reflections between phases. The apparent velocities of these arrivals were also used in the starting model for velocity analysis. Below we describe the identification of P- and S-wave phases in more detail and the production of velocity models from these interpretations.

Interpretation of P-wave arrivals

P-wave refractions could be readily identified on all instruments up to a maximum source-receiver offset of ~5-6 km. We have subdivided the P-wave refractions observed on Line 1 into four layers, not including the water column, based on changes in apparent velocity of similar arrivals (Fig. 3). Typically, apparent velocities for all observed sedimentary refractions varied from 3 to 5 km/s. Arrivals from the water column comprise direct arrivals from the shot to the receiver. These are observed only at very small offsets (< ~150 m) due to the shallow water depth (100 m) and have apparent velocities of ~1.5 km/s (picks in red on channel 2 in Fig. 3). Refractions from Layer 1 have apparent velocities of ~3-3.2 km/s and are observed at offsets up

to ~1-1.5 km (picks in orange on channel 2 in Fig. 3). Refractions from Layer 2 have apparent velocities of ~3.6-3.9 km/s and are observed at offsets between ~1 and 2.5 km (picks in yellow on channel 2 in Fig. 3). Refractions from Layer 3 have apparent velocities of ~4.1-4.5 km/s and are observed at offsets between ~1.5 and 3.5 km (picks in green on channel 2 in Fig. 3). Finally, refractions for Layer 4 have apparent velocities of ~4.6-5.0 km/s and are observed at offsets between ~3 to 6 km (picks in blue on channel 2 in Fig. 5). Wide-angle reflections were also observed on some instruments, but these were less common. Reflections from the bases of layers 1, 2 and 3 were each observed on two to three instruments. Picking uncertainties were between 8 and 12 ms for the refractions and 16 ms for the reflections.

Interpretation of S-wave arrivals

S-waves travel slower and arrive later than P-waves and thus can be identified by their later arrival times and lower apparent velocities. Additionally, they are often of comparatively high relative amplitude in data recorded on the horizontal components. We have interpreted up to four refracted S-wave phases on record sections from all instruments by comparing both horizontal and vertical geophone components (Fig. 3). These arrivals are interpreted to have converted from P- to S-waves at the seafloor based on the relatively small delay between P- and S-wave arrivals at small offsets. If these phases converted at a deeper interface, the implied near-surface S-wave velocities would be unrealistically low. These refractions have apparent velocities between 1.6-3.0 km/s, with refractions from Layer 1 having apparent velocities of ~1.6-1.7 km/s, refractions from Layer 2 having apparent velocities of ~1.9-2.1 km/s, refractions from Layer 3 having apparent velocities of ~2.3-2.5 km/s, and refractions from Layer 4 having apparent velocities of ~2.6-3.0 km/s. The picking errors for these phases were 12-20 ms. S-wave

phases are labeled on both the vertical and horizontal components of OBS 4 in Fig. 3 using the same color code as used for P-waves.

Velocity model construction by ray-tracing and forward modeling

An initial velocity model may be derived from these phase interpretations and their accompanying apparent velocity estimations. This initial model is then used as the basis for forward modeling of the observed traveltime picks. In this study, we have used the 2D ray-tracing and forward modeling package of Zelt and Smith (1992). For input into this package, the velocity model is specified in terms of a vertical and lateral mesh of nodes at which the velocity and depth are specified. Depth nodes define the layering, and velocity nodes define the velocity at the top and base of each of these layers and consequently the lateral and vertical velocity gradients within.

Rays are traced through this model, and the calculated traveltimes are compared with the observed, assessing the fit statistically within the assigned errors. The model is then iteratively adjusted in an attempt to improve the fit between observed and calculated traveltimes for all P- and S-wave reflections and refractions (Fig. 4). We adopted a top-down approach, modeling the shallowest layer before working downward progressively to deeper layers in a layer-stripping manner. We first created a 2D velocity model along Line 1 that fits the P-wave arrivals using the method described above. This model includes lateral variations in velocity and in the depths to boundaries between layers (Fig. 5). Interface geometries were modeled from wide-angle data alone (i.e., MCS data were not incorporated in modeling); variations in interface depth were based on limited wide-angle reflections and changes in the cross-over distance between different refracted phases.

We then created a 2D S-wave velocity model along the same line using interpreted S-wave refractions. In this model, the interfaces determined by modeling P-wave phases were held fixed, and only velocities within layers were modified to produce a good fit between observed and calculated S-wave phases. The rationale for leaving interfaces fixed from the P-wave model is that we have better constraints on variations in the depths to interfaces from the P-wave arrivals, which include both reflections and refractions. The starting S-wave velocity model had a constant V_P/V_S ratio of ~1.9 in all layers, a typical value for limestone (Pickett, 1963). We then tried to achieve an acceptable fit to the data by changing S-wave velocities as necessary. Following the creation of 2D P- and S-wave models along Line 1, we compared these models to both P- and S-wave arrivals from Line 2 that were observed on OBS 3, which lies at the intersection of these two lines. This comparison allowed us to check that the 2D model from Line 1 fit the data from Line 2 where the two lines intersect. Finally, we used the 2D P- and S-wave velocity models from Line 1 to compute the V_P/V_S ratio. The results of all of these analyses are described in the following section.

Results

V_P model

The V_P and V_S models along Line 1 comprise four layers (not including the water column) (Fig. 5) based on changes in the apparent velocity of P-wave refractions on each OBS record section (Fig. 3) and the observation of wide-angle reflections between some layers. The velocities within each of these layers increase with depth. In the P-wave velocity model, the shallowest layer (Layer 1) lies at depths of 100-220 m below OBS 3, and thickens to ~460 m

towards the north and south. Velocities in this layer are between 2.85-3.38 km/s. Layer 2 lies at depths of 220-490 m below OBS 3 and 460-650 m to the north and south; this layer has velocities of 3.6-3.85 km/s. Layer 3 lies at depths of 490 to 660 m beneath OBS 3 and 620-900 m to the north and south; this layer has velocities of 4.35-4.6 km/s. Finally, Layer 4 lies at depths greater than 660 m beneath OBS 3 and greater than 900 m towards the north and south; this layer has velocities of 4.60-5.20 km/s. This is the deepest layer, and it can be constrained to depths of approximately 1 km below the sea surface. Layers 2-4 appear to shallow towards the center of this profile (Fig. 5a), consistent with seismic reflection data in this region (Fig. 2b). Velocities within layers show different lateral trends. In Layers 1, 2 and 4, P-wave velocities decrease towards to south, but in Layer 3, they increase towards the south (Fig. 6). The data fit for this model is good; it has a normalized χ^2 value (misfit weighted by picking error) of 0.760; a value of 1.0 is considered an acceptable fit. The root-mean-squared (RMS) traveltime residual is 10 ms; 4759 picks were included in this analysis. Lateral variations in all layers but Layer 2 are ≥0.2 km/s, and are thus significant based on uncertainty tests described below, which showed that velocities in our final model can be determined with an uncertainty of approximately ±0.03 km/s. Likewise, interface depths in our final model vary laterally by approximately 200-300 m, and such variations are thus significant considering uncertainties of ±40 m in boundary depths.

V_S model

The interfaces in the S-wave velocity models are identical to those in the P-wave model; only the velocities have been changed to obtain a fit (Fig. 5b). As described earlier, interfaces were left fixed from the P-wave model because P-wave arrivals include wide-angle reflections that provide better constraints on the shapes and depths of interfaces. On Line 1, S-wave

velocities in Layer 1 are nearly constant at 1.51-1.53 km/s. Layer 2 has S-wave velocities of 1.75 to 1.99 km/s; velocities decrease laterally from 1.87-1.99 km/s in the north to 1.75-1.95 km/s in the south. Layer 3 has S-wave velocities of 2.24-2.55 km/s. Like Layer 2, velocities in Layer 3 decrease laterally from 2.45-2.55 km/s in the north to 2.24-2.30 km/s in the south. Layer 4 has S-wave velocities of 2.43-2.83 km/s. As in Layers 2 and 3, velocities within Layer 4 also appear to decrease from north to south, although this change is only constrained by arrivals on one instrument. If correct, this implies a lateral change from 2.68-2.83 km/s in the north to 2.43-2.53 km/s in the south. This model also fits the data well, although the misfits are slightly higher than those for the V_P model. The final model fit is based on 1371 traveltime picks, has a normalized χ^2 value of 1.708 and an RMS traveltime residual of 22 ms. The relatively high normalized χ^2 value is most likely a result of the assignment of picking uncertainties that were too small, when considered in terms of the ability to pick phase traveltimes when the phases in question are second arrivals and hence embedded in the wave-train of the preceding P-wave arrivals. Lateral variations in S-wave velocity within Layers 3 and 4 are considered significant because they are greater than estimated uncertainties of ±0.03 km/s described below.

V_P/V_S models

The V_P/V_S ratio calculated from these velocities varies between layers and laterally along Line 1 within individual layers. Layer 1 is characterized by V_P/V_S values of ~1.9-2.2, Layer 2 by values of 2-2.05, Layer 3 by values of 1.8-1.95, and Layer 4 by values of 1.85-2.0. In all of the layers except Layer 1, V_P/V_S increases from north to south (Figs. 5c and 6). We feel confident about these variations within Layers 1-3, but the lateral variations in Layer 4 are the least well constrained. As described below, S-wave velocities in the deepest layer are only constrained by

arrivals observed on one instrument. But if these are correct, Layer 4 shows a sharp change in V_P/V_S 2 km to the south of OBS 3 (Fig. 5).

Resolution and imaging

It is important to emphasize the limitations of these models before discussing their interpretation. Firstly, portions of the Line 1 model to the north of OBS 1 and to the south of OBS 6 are poorly constrained because the arrivals from shots fired along these parts of the line are unreversed, leading to uncertainties in the velocities determined if there are dipping layers or other 2D (or 3D) features in the subsurface. For this reason only the central section of the model is presented in Fig. 5 and described in the text. Secondly, because these models were created from only three pairs of OBSs spaced at 1.6 km intervals, there are significant limits on the spatial resolution even in the central portion of the model. As a result, we attempted to construct as simple a model as possible, introducing lateral variations in velocity or in the depths to interfaces only when necessary. Consequently, nodes in the model are sparsely spaced at between ~1-2 km horizontally, and 0.1-0.2 km vertically. The scale lengths of such variations are similar to the spacing of the OBSs, which provides an approximate estimate of lateral resolution (Zelt, 1999).

Some layers in the P- and S-wave velocity models are better constrained that others due to the number of P- and S-wave arrivals observed for each layer. There are fewer limitations on individual layers within the P-wave model because arrivals from all four layers were observed both to the north and south of all six instruments (Figs. 3 and 4). Nonetheless, picking uncertainties increase with increasing source-receiver offset (e.g., from 8 to 12 ms for P-wave refractions), so that the deepest layers are slightly less well resolved than the shallow layers.

322 More variability in constraints exists for the S-wave model. Overall, the S-wave velocity
323 structure is less well constrained than the P-wave velocity structure; fewer phases were observed
324 and interpreted, and where they were interpreted, higher picking uncertainties are associated with
325 them compared with P-wave phases. Even though S-wave arrivals from all of the layers are
326 recorded on at least four of the six instruments, these are not always observed to both the north
327 and south of all instruments or over a broad range of offsets. As a result, reversed coverage of
328 the central portion of the model space is more variable (Fig. 4). The layer with the fewest
329 arrivals and the largest picking uncertainties is Layer 4. Specifically, the S-wave velocity
330 structure in Layer 4 in the southern portion of the model is only constrained by unreversed
331 arrivals from one instrument (offset 16 km, Fig. 4c), making it the most poorly constrained part
332 of the model.
333 We have tested the sensitivity of our data fit to changes in layer velocities and interface
334 depths in two different ways. Firstly, we perturbed all of the velocities within a layer or all of the
335 depths to the base of the layer and determined the amount of perturbation (either in terms of
336 percent change to velocity or change in depth, respectively) that led to a model with a χ^2 value
337 greater than one. Secondly, we applied the F-test of Zelt and Smith (1992), which uses both the
338 number of picks and χ^2 value to calculate the probability that the models are significantly
339 different. The F-test yielded smaller uncertainties than simply comparing χ^2 values, so we report
340 the larger uncertainties suggested by the latter here. This test shows that P-wave velocities
341 within these layers can be varied by only ±1% (e.g.,±0.03-0.04 km/s) and still produce
342 acceptable data fits (e.g., χ^2 values less than one). S-wave velocities appear to be similarly
343 constrained based on the shape of the velocity perturbation versus data fit function, although this
344 is more difficult to assess because data misfits associated with the best-fitting S-wave model

have a χ^2 value greater than one. Data fit is less sensitive to variations in interface depths because they are only constrained by limited wide-angle reflections and cross-over distances between different refracted phases. The shallowest two interfaces can be varied by as much as ±20 m and still produce acceptable data fits. However, the boundary between layers 3 and 4 can be varied by ±40 m.

Another limitation of our model is the range of depths that can be constrained. Our model only extends to a total depth of approximately ~1 km due to the apparent disappearance of first arrivals at offsets of 5-6 km. As a consequence, variations in P- and S-wave velocity associated with deeper reservoir rocks (e.g., Wealden sands) could not be determined. There are several explanations for the absence of arrivals from larger offsets, which include: 1) limited signal penetration or 2) the existence of a thick low-velocity zone. Signal penetration problems can arise if the seismic source is of insufficient amplitude or does not contain enough energy at appropriate frequencies for propagation to the required depths of investigation. The airgun source used in this experiment had a total volume of 470 in^3, and the guns were towed at 4 m, which would favor relatively high frequencies appropriate for a shallow survey of this kind. However, both the volume and frequency content of this seismic source should have been sufficient to penetrate at least 4-5 km into the subsurface based on pre-cruise source modeling by Gardline Geosurvey Ltd. Consequently, this explanation appears unlikely.

The alterative explanation is the presence of a low-velocity zone. In this case, the apparent disappearance of arrivals at offsets of 5-6 km might represent a shadow zone commonly associated with thick low velocity zones. Seismic waves that encounter velocities lower than those from which they came are not refracted back towards to surface until they encounter higher velocities again, which creates a “step back” in arrivals. Preliminary modeling implies that a

thick (~1.5 km) low velocity zone beneath the base of our deepest layer (~1-1.25 km) could explain the disappearance of first arrivals. Sonic velocities from well logs also support this possibility. At 49/26-1A (Fig. 1), velocities decrease from ~5.08 km/s at a depth of 950 m to ~3.39 km/s at a depth of 967 m. Velocities as high as 5.08 km/s are not seen throughout the rest of the logged interval (total depth of 1892 m). These data suggest the existence of a low velocity zone whose thickness is at least 1 km, if not more.

Discussion

The velocity models presented in this study, particularly the V_P/V_S ratio, provide new constraints on possible variations in subsurface physical properties in the upper 1 km of sediments at the Blackrock prospect in the North Celtic Sea Basin. The V_P/V_S ratio is more sensitive to variations in lithology, porosity and pore-fluid content than V_P or V_S alone, making it a useful parameter for evaluating hydrocarbon prospects. This work demonstrates the ability of a relatively cheap and time-efficient method, an OBS survey, to recover lateral variations in V_P, V_S, and the V_P/V_S ratio in this environment. All of these implications are described in greater detail in the sections below.

Application of OBSs to study of the V_P/V_S ratio

The most important result of this study is that we have demonstrated the ability of an OBS survey consisting effectively of only three instrument sites, deployed over a total distance of 3.5 km, to recover lateral variations in V_P, V_S, and the V_P/V_S ratio using mode-converted S-waves. The geology of the North Celtic Sea Basin is ideal for such a study because the contrast in physical properties resulting from the hard seabed favors the generation of converted S-waves.

391 The primary advantage of this approach is that the data are relatively cheap and quick to collect
392 and analyze. One disadvantage of the simple survey geometry and, particularly, the sparse
393 instrument coverage used for the survey presented here, is that only coarse variations in
394 subsurface properties can be detected. To increase lateral resolution, more OBSs would be
395 required. However, the cost of adding additional seismographs to the survey is small compared
396 to the mobilization and operational costs of the vessel and the airgun array required for shot
397 firing, and the streamer required if contemporaneous MCS data acquisition is desired.
398 Consequently, higher resolution studies could be conducted without large additional costs.
399 Another improvement on the study presented here would be to conduct a 3D OBS survey. Given
400 that hydrocarbon systems, themselves, are three dimensional, the deployment of OBS and
401 generation of seismic sources over a small 3D region would allow for more sophisticated
402 modeling, such as 3D tomographic inversion, to estimate 3D changes in P- and S-wave structure
403 at depth. Such a 3D survey would add significant value to the outcomes of analysis without
404 incurring much additional cost.
405
406 ***V_P and V_S structure***
407 The P- and S-wave velocity models consist of 4 layers based on variations in the apparent
408 velocity of P-wave refractions. The velocities observed throughout the P-wave model are much
409 higher than average values derived from global compilations of marine sedimentary rocks, which
410 are commonly between 1.5-2.2 km/s (Hamilton, 1978). Likewise, velocities in our S-wave model
411 are also much higher than those in global compilations, which are typically << 1.5 km/s in
412 shallow marine sediments (Hamilton, 1979). This implies that the sedimentary rocks within the
413 modeled depth range have already experienced a significant reduction in porosity via compaction

414 and/or cementation; the principle compaction mechanism in the North Celtic Sea Basin is
415 thought to be burial (Hillis, 1991; Murdoch *et al*., 1995). As a result, the most likely explanation
416 for high velocities in the shallow subsurface is that younger, less consolidated sediments were
417 removed during Cenozoic uplift events, exposing deeper more indurated sedimentary rocks.
418 Maps of regional net uplift created by Murdoch *et al*. (1995) suggest that the area of the
419 Blackrock prospect experienced approximately 400-700 m of net uplift.

420 As described in the results section, Layers 2-4 appear to shallow towards the center of
421 Line 1, reaching their shallowest level at an offset of ~12 km (Fig. 5). Similar features can be
422 observed in both regional seismic lines and coincident MCS data along Line 1 (Figs. 2 and 7).
423 Folded Layers 2-4 are overlain by Layer 1, which thickens to the north and south as Layers 2-4
424 deepen. This pattern could either suggest that Layer 1 has been deposited in the accommodation
425 space remaining following uplift and folding of Layers 2-4 or that Layer 1 is also folded, but the
426 apex of this fold has been eroded. The velocities within Layer 1 are too high to represent
427 sediments that have not experienced significant reduction in porosity, so we favor the later
428 possibility. Interpretations of MCS data by Providence Resources suggest that this folded
429 structure is bound by faults to the northwest and southeast; these faults dip inward beneath the
430 fold (Figs. 2 and 7). These features are most likely inversion structures related to uplift
431 associated with the North Atlantic Volcanic Province and Alpine Orogeny; such structures are
432 observed elsewhere throughout the North Celtic Sea Basin (Murdoch *et al*., 1995; Shannon and
433 Naylor, 1998).

434 By comparing our models with drilling results and interpretations of seismic stratigraphic
435 sequences presented in Figs. 2 and 7, constraints can be placed on the correspondence between
436 layers in our velocity model and stratigraphic units. From this comparison, it appears likely that

Layer 1 comprises both a thin Cenozoic sedimentary succession and the top of Upper Cretaceous chalks (Fig. 7). Cenozoic sediments are likely Eocene-Oligocene in age, as most of the Paleocene section was removed during uplift associated with the North Atlantic Igneous Province. Drilling at 49/26-1A encountered the top of the Upper Cretaceous chalks at 127 m, which is only ~25 m below the seafloor, implying that most of Layer 1 corresponds to chalks. We also interpret our Layers 2-4 as corresponding primarily to Upper Cretaceous chalks. The high P- and S-wave velocities observed in Layers 1-4 are consistent with this interpretation. Murdoch *et al.* (1995) have subdivided Upper Cretaceous chalks in the North Celtic Sea Basin into four sub-units based on variations in their resistivity and velocity characteristics from well logs; similarly, the subdivision of Upper Cretaceous chalks into four layers in our velocity model appears to indicate variations in physical properties within this unit. During drilling at 49/26-1A, the rate of penetration slowed at 499.8 m, which was interpreted as a possible contact between upper and lower units of the Upper Cretaceous chalks; this level corresponds to the base of our Layer 1, providing further evidence of the subdivision of Upper Cretaceous chalks with respect to physical properties. The velocities observed in Layer 4 from the modeling discussed earlier (4.60-5.20 km/s) closely match the average velocity of 4.97 km/s given for the deepest sub-unit of the chalk described by Murdoch *et al.* (1995) for this area.

By time converting our P-wave velocity model, it is evident that the base of our model roughly corresponds to the "base chalk" layer interpreted by Providence Resources, although Layer 4 might encompass a portion of the underlying Cenomanian and Albian limestones and mudstones (e.g., at ~11.75 and 13.5 km offset in Fig. 7). Drilling at 49/26-1A gave a depth of 921 m to the base of the Upper Cretaceous chalks and a total thickness of ~800, suggesting that the deepest 100-200 m of Layer 4 encompasses underlying layers (Fig. 5). Well logs from 49/26-

460 1A and 48/30-1 suggest that these units have velocities of ~4.4-5.1 km/s, which are also similar
461 to those observed in Layer 4.
462
463 ***V_P /V_S structure***
464 Overall, the V_P/V_S ratios throughout the V_P/V_S model are relatively low (1.8-2.2)
465 compared to those associated with global compilations of marine sedimentary rocks at these
466 depths, which can have values of V_P/V_S as high as 13.0 near the seafloor (Hamilton, 1979). The
467 V_P/V_S ratio increases with increasing porosity, suggesting that sedimentary rocks modeled in the
468 present analysis have relatively low porosities due to burial compaction and subsequent removal
469 of shallower sediments during the Cenozoic, as discussed in the previous section. On a gross
470 scale, the V_P/V_S ratio decreases with depth. This is a common feature in sedimentary sections and
471 is usually attributed to increasing compaction and the associated loss of porosity (Hamilton,
472 1979; Mjelde *et al*., 2003). As described in the previous section, we have correlated most of
473 Layers 1-4 to Upper Cretaceous chalks, except for the uppermost ~25 m of Layer 1 and
474 lowermost 100-200 m of Layer 4. The V_P/V_S ratios in these layers of 1.8-2.1 are reasonable for
475 limestones, which typically have values of ~1.85-1.95 (Pickett, 1963).
476 In the deepest two layers, V_P/V_S appears to increase towards the south by approximately 0.1-0.2
477 (Fig. 6). These lateral changes are relatively well constrained in Layer 3, but less certain in Layer
478 4 because they are only sampled there by one phase. North-south variations in V_P/V_S observed in
479 Layers 3 and 4 could either result from lateral changes in lithology, porosity or pore fluids.
480 Sandstones and limestones typically have lower V_P/ V_S ratios than shale, so changes in the clay
481 fraction, for example, might account for a lateral variation in the V_P/V_S ratio. However, we
482 consider this explanation unlikely because drilling in this area does not suggest significant lateral

variations in lithology over only a few kilometers. An alternative explanation is that the southward increase in the V_P/V_S ratio is caused by a southward increase in porosity; the V_P/V_S ratio increases with increasing porosity (Hamilton, 1979). A ~10 percent decrease in porosity would be required to achieve a 0.2 change in the V_P/V_S ratio for a water-saturated rock (Gregory, 1976). We also consider this explanation unlikely as well log data from 48/30-1 and 49/26-1A indicate porosity variations of only ~3-5 percent in the uppermost logged interval (>900 m, Cenomanian and Albian units). Finally, the third possible explanation for the change in the V_P/V_S ratio is a change in pore fluid contents; the presence of hydrocarbons, particularly gas, tends to cause a decrease the V_P/V_S ratio (Gregory, 1976). While the V_P/V_S ratios observed in Layers 3 and 4 are somewhat higher than would be expected for a rock whose entire pore space is occupied by gas (Gregory, 1976), the lateral variation could be attributed to an increasing percentage of gas versus water in rocks containing both phases. Additionally, samples used by Gregory (1976) for his laboratory work did not include shales, which usually have higher V_P/V_S ratios than sandstones or limestones; the possible presence of shales at the base of Layer 4 might result in a higher overall V_P/V_S ratio even in the presence of gas. Increased gas accumulations have been observed in the units overlying hydrocarbon-bearing reservoir rocks at structural highs; this interpretation would explain the observations we see in this location. Analysis of canned cuttings and core samples for hydrocarbons at 48/30-1 indicated the presence of gas and minor oil in the Albian/Aptian, while no gas was observed in these units to the south at 49/26-1A. Although our model does not extend to depths equivalent to the reservoir, the northward decrease in the V_P/V_S, together with well results, would appear to be a positive sign that the results of drilling to the north of the basin shoulder fault might be more successful.

Conclusions

The most important result of this study is that we have demonstrated the ability of an OBS survey consisting effectively of only three instrument sites, deployed over a total distance of 3.5 km, to recover lateral variations in V_P, V_S, and the V_P/V_S ratio in shallow sedimentary rocks using mode-converted S-waves. The geology of the North Celtic Sea Basin is ideal for such a study because the contrast in physical properties resulting from the hard seabed favors the generation of mode-converted S-waves. The primary advantage of this approach is that the data are relatively cheap and quick to collect and analyze compared with ocean-bottom cables.

The purpose of this study was to determine the V_P/V_S ratio of consolidated sedimentary rocks at the Blackrock prospect in order to constrain possible subsurface variations in pore-fluid content. Our P- and S-wave velocity models consist of four layers and extend to a maximum depth of 1.1 km. Layers 2-4 appear to shallow towards the center of the profile, forming a fault-bound inversion structure that is a target of current hydrocarbon exploration. Both P- and S-wave velocities are exceptionally high for sedimentary rocks at these depths; this is likely explained by the removal of shallower strata during Cenozoic uplift events (Murdoch *et al.*, 1995). These layers are interpreted to primarily represent Upper Cretaceous chalks, except for the uppermost 25 m of Layer 1 and lowermost 100-200 m of Layer 4. The V_P/V_S ratio calculated from the P- and S-wave velocity models contains values of 1.8-2.1, consistent with typical values for limestones. Northward decreases in the V_P/V_S ratio are observed in the deepest two layers; we interpret this to indicate increased gas in the pore-space towards the north across an interpreted basin-bounding fault. The modeled region extends to a maximum depth of 1.1 km, a limitation imposed by the disappearance of refractions at source-receiver offsets of ~5-6 km. A thick low-

528 velocity zone beneath ~1.2 km depth is our preferred explanation, which is supported by logging
529 data from 49/26-1A and predictive modeling.

Acknowledgements

We gratefully acknowledge A.C. Burchell and J. McIntosh, the OBIC engineers responsible for OBS data acquisition, Gardline Geosurvey Ltd. and Providence Resources employees involved in the planning and acquisition, and the crew of the M/V *Sea Surveyor*. We would particularly like to thank Fergus Roe (Providence) and Richard Thompson (Gardline), for their feedback on the collection and interpretation of these data, and Gavin Elliot for useful discussions about geology of the North Celtic Sea Basin. This work was a research collaboration with Providence Resources and its partners, DYAS BV, Challenger Minerals (Celtic Sea) Limited, ForestGate Resources Inc., Atlantic Petroleum (Ireland) Limited, and was supported by Gardline Geosurvey, Ltd.

References

Garotta, R., P.-Y. Granger, and H. Dariu, 2002, Combined interpretation of PP and PS data provides direct access to elastic rock properties: Leading Edge, v. 21, p. 532-535.

Gregory, A. R., 1976, Fluid saturation effects on dynamic elastic properties of sedimentary rocks: Geophysics, v. 41, p. 895-921.

Hamilton, E. L., 1978, Sound velocity-density relations in sea-floor sediments and rocks: J. Acoust. Soc. Am., v. 63, p. 366-377.

Hamilton, E. L., 1979, V_p/V_s and Poisson's ratios in marine sediments and rocks: J. Acoust. Soc. Am., v. 66, p. 1093-1101.

Hillis, R. R., 1991, Chalk porosity and Tertiary uplift, Western Approaches Trough, SW UK and NW French continental shelves: J. Geol. Soc. London, v. 148, p. 669-678.

Hughes, S., P. J. Barton, and D. Harrison, 1998, Exploration in the Shetland-Faeroe Basin using densely spaced arrays of ocean-bottom seismometers: Geophysics, v. 63, p. 490-501.

Jin, S., G. Cambois, and C. Vuillermoz, 2000, Shear-wave velocity and density estimation from PS-wave AVO analysis: Application to an OBS dataset from the North Sea: Geophysics, v. 65, p. 1446-1454.

Knapp, S., N. Payne, and T. Johns, 2002, Imaging through gas clouds; case histories from the Gulf of Mexico: Annual Meeting Expanded Abstracts - AAPG, v. 2002, p. 95.

Mjelde, R., T. Raum, P. Digranes, H. Shimamura, H. Shiobara, and S. Kodaira, 2003, Vp/Vs ratio along the Vøring Margin, NE Atlantic, derived from OBS data: implications on lithology and stress field: Tectonophysics, v. 369, p. 175-197.

Murdoch, L. M., F. W. Musgrove, and J. S. Perry, 1995, Tertiary uplift and inversion history in the North Celtic Sea Basin and its influence on source rock maturity, *in* P. F. Croker, and P. M. Shannon, eds., The Petroleum Geology of Ireland's Offshore Basins, Geological Society Special Publication, v. 93: London, Geological Society, p. 297-319.

Ó Cofaigh, C., and D. J. A. Evans, 2007, Radiocarbon constraints on the age of the maximum advance of the British-Irish Ice Sheet in the Celtic Sea: Quaternary Science Reviews, v. 26, p. 1197-1203.

Pickett, G. R., 1963, Acoustic character logs and their application in formation evaluation: J. Petr. Tech., p. 659-667.

Rowell, P., 1995, Tectono-stratigraphy of the North Celtic Sea Basin, *in* P. F. Croker, and P. M. Shannon, eds., The Petroleum Geology of Ireland's Offshore Basins, Geological Society Special Publication, v. 93: London, Geological Society, p. 101-137.

Roy, I. G., M. K. Sen, C. Torres-Verdin, and O. J. Varela, 2002, Pre-stack inversion of a Gulf of Thailand OBC data set: SEG Annual Meeting Expanded Technical Program Abstracts, v. 72, p. 914-917.

Shannon, P. M., and D. Naylor, 1998, An assessment of Irish offshore basins and petroleum plays: J. Petrol. Geol., v. 21, p. 125-152.

Spitzer, R., R. S. White, and iSIMM Team, 2005, Advances in seismic imaging through basalts: A case study from the Faroe-Shetland Basin: Petroleum Geoscience, v. 11, p. 147-156.

Spudich, P., and J. Orcutt, 1980, A New Look at the Seismic Velocity Structure of the Oceanic Crust: Reviews of Geophysics and Space Physics, v. 18, p. 627-645.

Taber, D. R., M. K. Vickers, and R. D. J. Winn, 1995, The definition of the Albian 'A' Sand reservoir fairway and aspects of associated gas accumulations in the North Celtic Sea Basin, *in* P. F. Croker, and P. M. Shannon, eds., The Petroleum Geology of Ireland's

Offshore Basins, Geological Society Special Publication, v. 93: London, Geological Society, p. 227-244.
Tatham, R. H., 1985, Shear waves and lithology, *in* G. Dohr, ed., Seismic Shear Waves: Part B., Applications: London, Geophysical Press, p. 86-133.
Zelt, C. A., 1999, Modelling strategies and model assessment for wide-angle seismic traveltime studies: Geophys. J. Int., v. 139, p. 183-204.
Zelt, C. A., and P. J. Barton, 1998, Three-dimensional seismic refraction tomography: A comparison of two methods applied to data from the Faroe Basin: J. Geophys. Res., v. 103, p. 7187-7210.
Zelt, C. A., and R. B. Smith, 1992, Seismic traveltime inversion for 2-D crustal velocity structure: Geophys. J. Int., v. 108, p. 16-34.

Figure Captions

Figure 1. Map of study area showing the locations of shot lines, OBSs and nearby wells. The approximate location of an interpreted basin bounding fault is indicated with a thick black line. The inset in the upper right hand corner shows regional bathymetry from GEBCO and the location of Blackrock with respect to Ireland. The inset in the lower right hand corner shows a close up of instrument locations and squares shot around pairs of instruments, which were used to relocate the instruments and orient the horizontal sensors relative to shot lines.

Figure 2. **a.** Simplified stratigraphy of North Celtic Sea Basin after Shannon and Naylor (1998). **b.** Interpretation of a seismic reflection line across the Blackrock prospect, including interpretations of key stratigraphic horizons (Base of Chalk, top of Wealden sandstone, etc.) and faults; see text for details. The interpreted basin bounding fault is shown in bold. The projected location of 48/30-1 is indicated with a dashed black line, and the location of 49/26-1A with a solid black line. A large black arrow indicates the proposed location of future drilling.

Figure 3. Data example from OBS 4, which lies close to the center of Line 1 (Fig. 1). Data recorded on the vertical component of the geophone are shown on the left and data from the radial horizontal component of the geophone are shown on the right. Reduction velocities of 4 and 2.5 km/s have been applied to the vertical and horizontal component data, respectively, to facilitate phase identification. The upper panels show data without interpretation. The lower panels show interpreted phases color-coded by phase; see text for details. Both P- and S-wave arrivals are marked on the vertical component data, while only S-wave phases are indicated on

the horizontal component data. Direct arrivals through the water column are plotted in red (Layer 1). Arrivals from Layers 1, 2, 3 and 4 are indicated in orange, yellow, green and blue, respectively. The apparent increased amplitude between offsets of –4000 and –1500 m is due to the fact that this offset interval was shot twice and thus is more densely sampled. The vertical component data are plotted with a reduction velocity of 4 km/s to aid phase identification, while the horizontal component data are plotted at 2.5 km/s to reflect the slower phase velocities.

Figure 4. Ray diagrams and comparisons between observed and calculated picks for all P-wave (upper two panels) and S-wave (lower two panels) arrivals analyzed to create models shown in Fig. 5. **a.** Diagram of rays traced through the subsurface to create the P-wave model (Fig. 5a). Rays are color-coded by phase as in Fig. 3, with direct arrivals indicated in red, refractions in Layer 1 in orange, refractions in Layer 2 in yellow, refractions in Layer 3 in green, and refractions in Layer 4 in blue. Reflections from the base of Layers 1, 2, and 3 are shown in light orange, light yellow and light green, respectively. Layer boundaries are indicated with black dashed lines. Note that ray coverage is best between 10-14 km offset. **b.** Observed and calculated picks for the P-wave model. Observed picks are plotted as colored bars whose lengths represent the assigned picking error, and their colors are the same as those of corresponding rays in Fig. 4a. Black lines indicate arrivals calculated from the model. **c.** Diagram of rays traced through the subsurface to create S-wave model (Fig. 5b). The ray and model boundaries are labeled and colored as in Fig. 4a. **d.** Observed and calculated picks for the S-wave model. Picks are labeled and colored as in Fig. 4b.

Figure 5. a. P-wave velocity (V_P) model along Line 1. OBS locations indicated with white inverted triangles. Velocities contoured at 0.1 km/s intervals. Layers are labeled; see text for more detailed description. **b.** S-wave velocity (V_S) model along Line 1, labeled and colored in the same manner as in Fig 5b. **c.** V_P/V_S ratio along Line 1, calculated using velocity models in parts 5a) and 5b), is contoured at 0.05 intervals.

Figure 6. North-south variations in average V_P, V_S, and V_P/V_S within each model layer. Note that V_P decreases towards the south in all layers except Layer 3, and V_S decreases towards the south in all layers. V_P/V_S increases to the south in all layers except Layer 1.

Figure 7. a. Coincident MCS data along Line 1. **b.** Overlay of coincident MCS data on the time-converted V_P model. Interfaces between layers from the velocity models shown in Fig. 5 are indicated with red dashed lines. Well locations are indicated with solid red lines, interpreted faults with black solid lines, and stratigraphic interpretations with solid colored lines (provided by Providence Resources). **c.** Same as Fig. 7b, but with the V_P/V_S model.

Figure 1 - Shillington, Minshull, Peirce, O'Sullivan

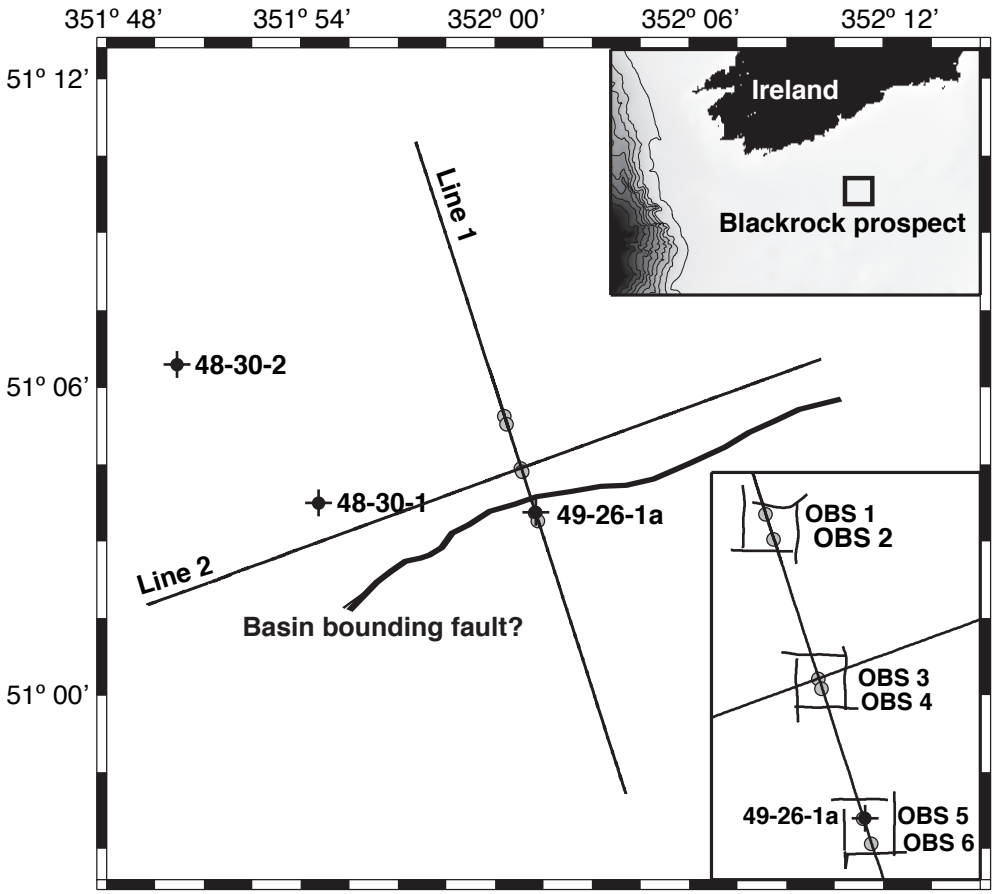

Figure 2 - Shillington, Minshull, Peirce, O'Sullivan

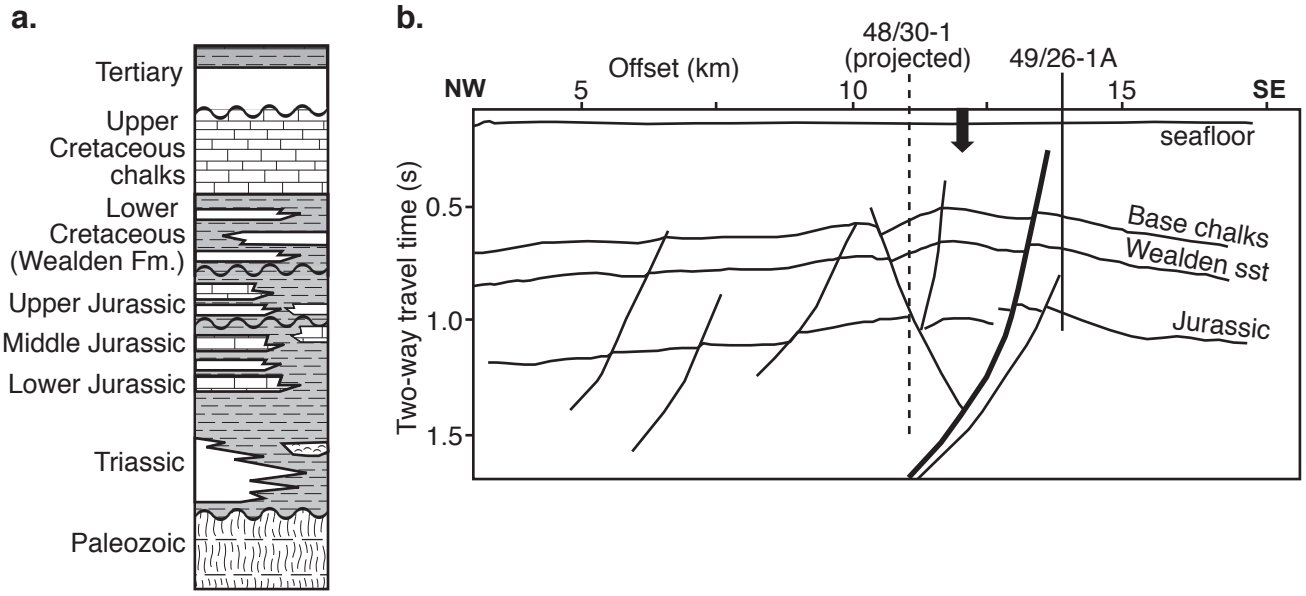

Figure 3 - Shillington, Minshull, Peirce, O'Sullivan

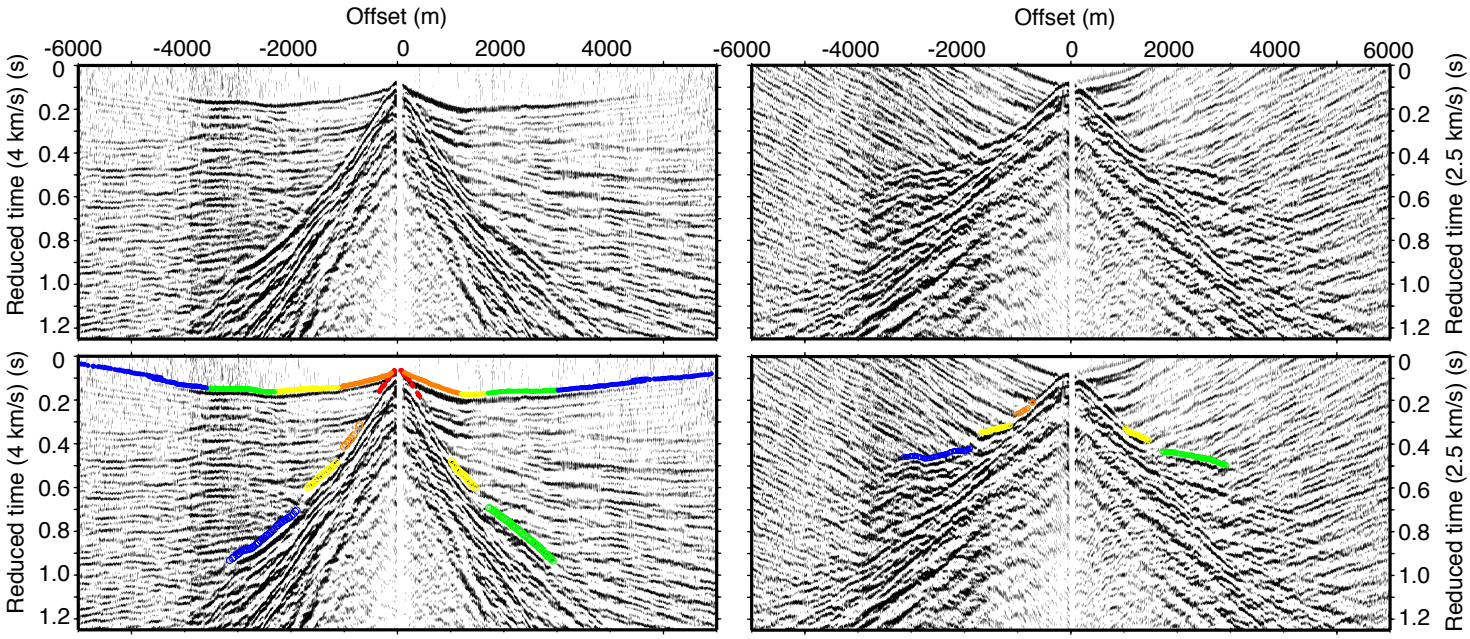

Channel 2, vertical component **Channel 3, radial horizontal component**

Figure 4 - Shillington, Minshull, Peirce, O'Sullivan

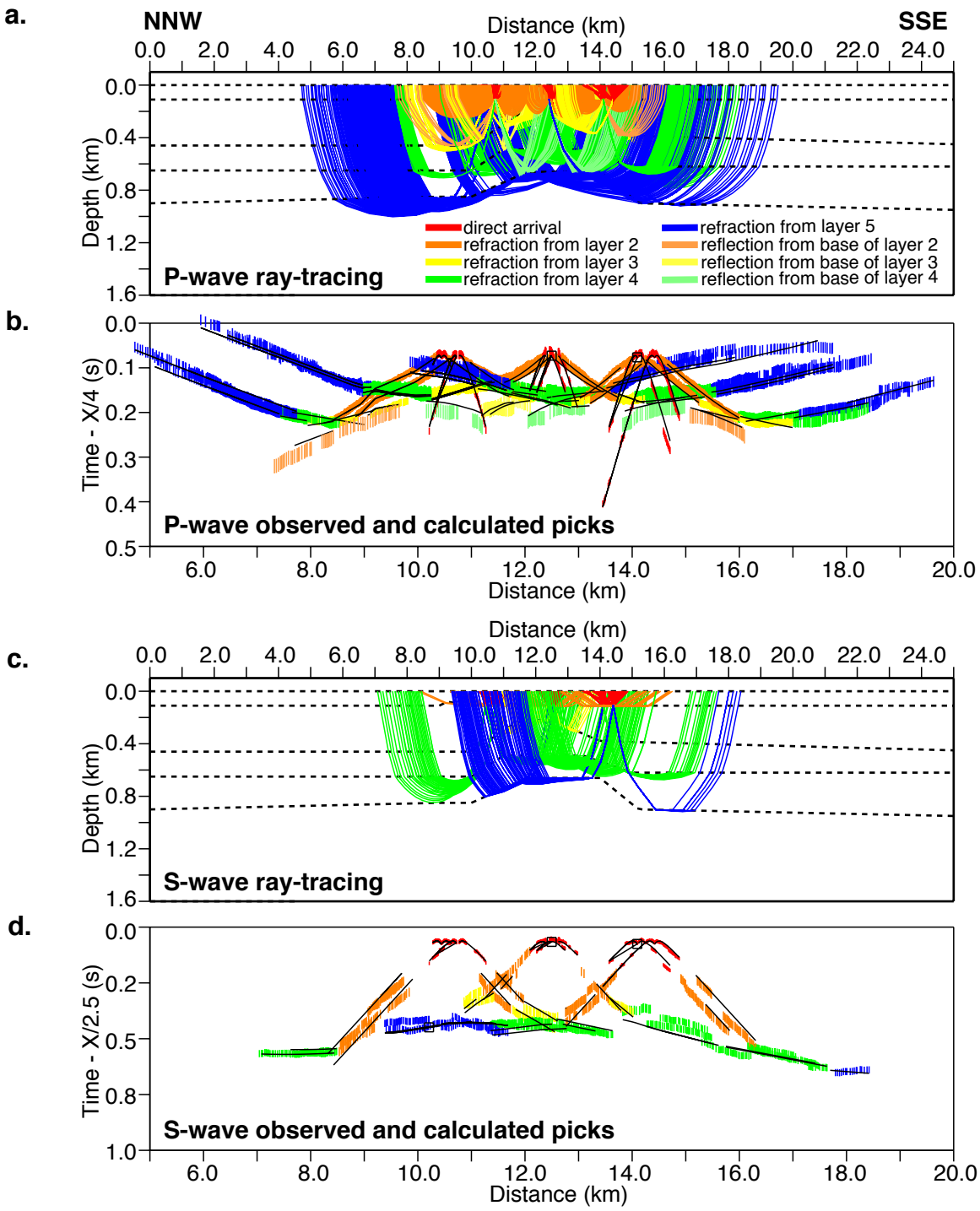

Figure 5 - Shillington, Minshull, Peirce, O'Sullivan

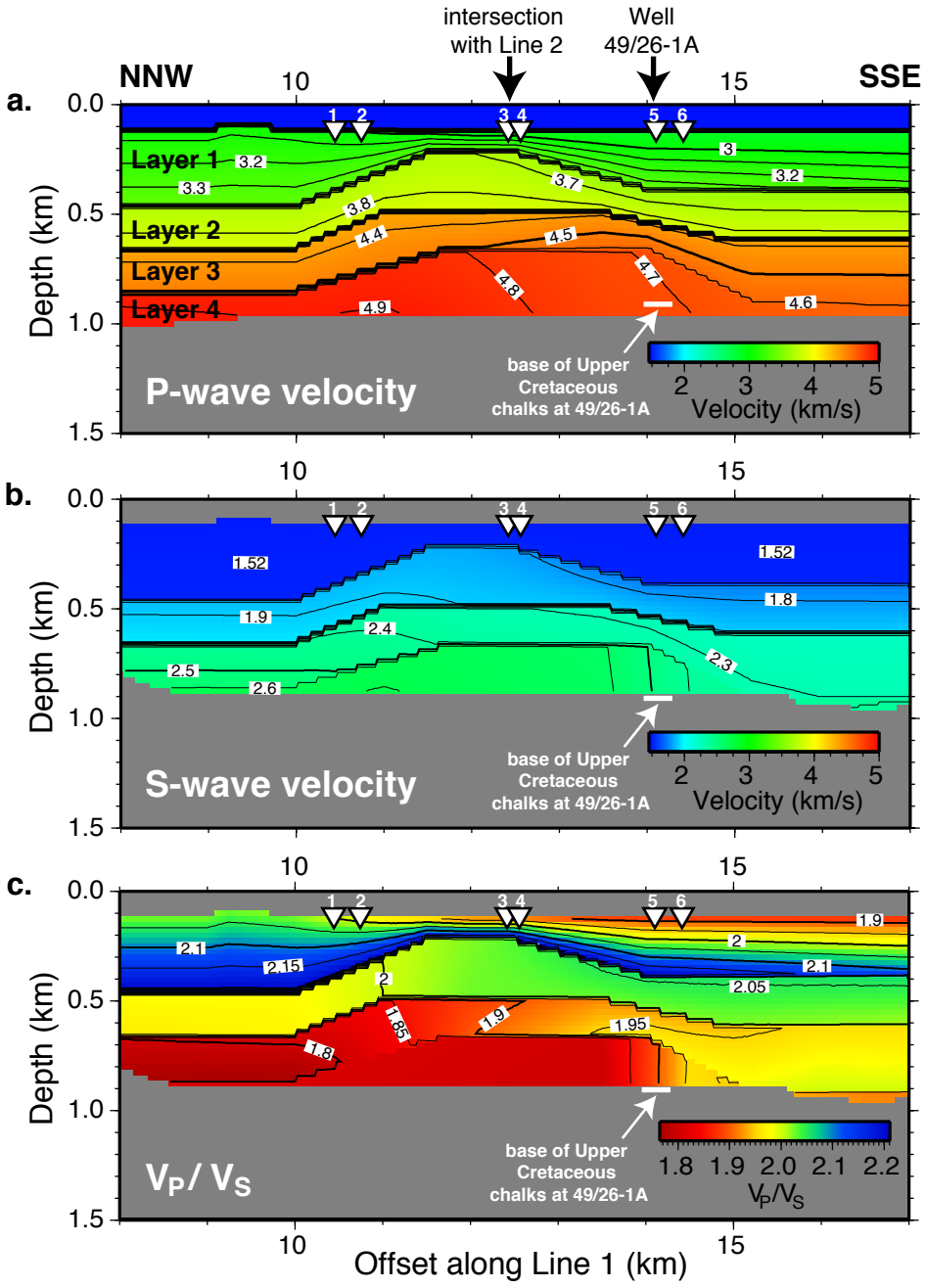

Figure 6 - Shillington, Minshull, Peirce, O'Sullivan

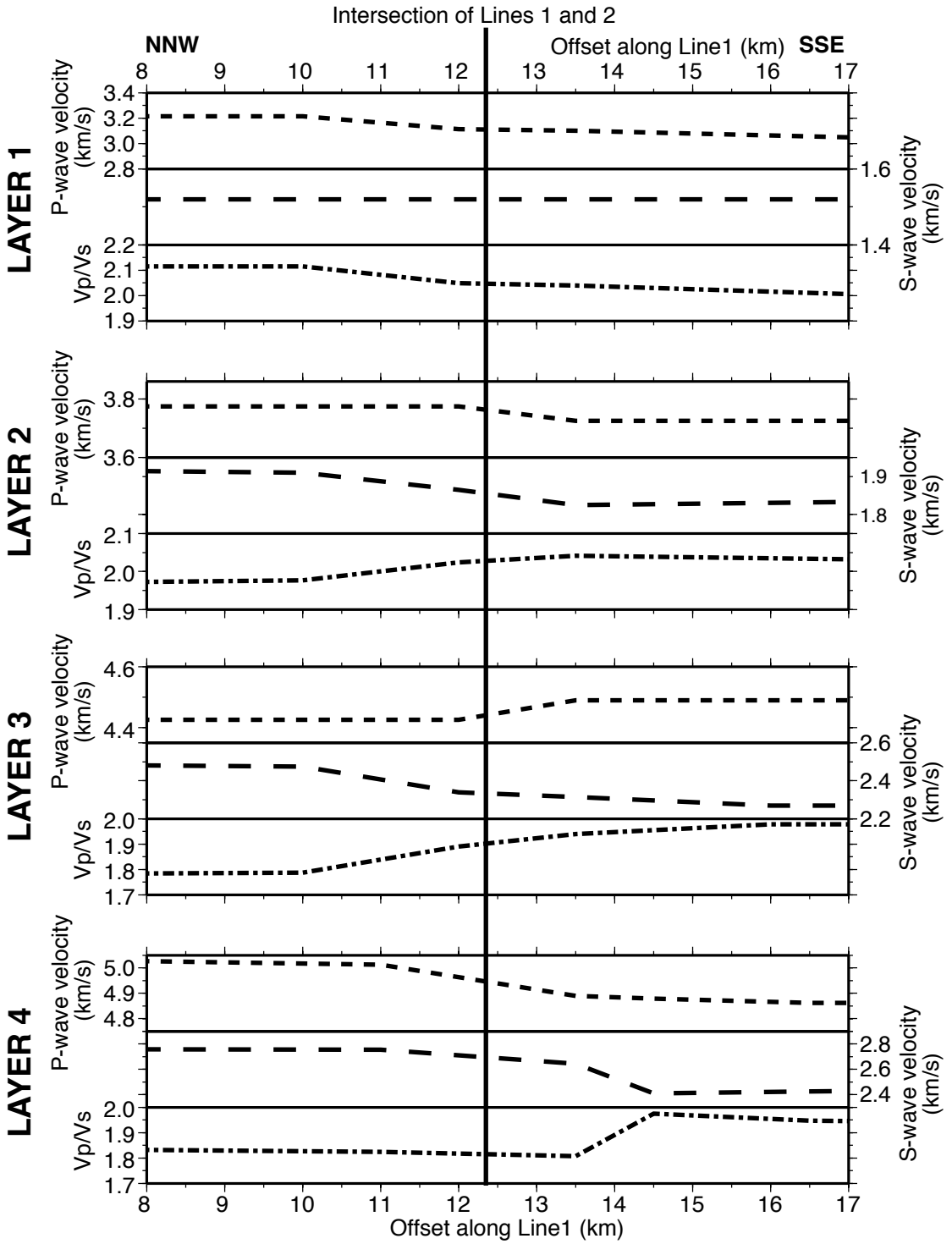

Figure 7 - Shillington, Minshull, Peirce, O'Sullivan